Available online at www.sciencedirect.com

ScienceDirect

journal homepage: www.elsevier.com/locate/he

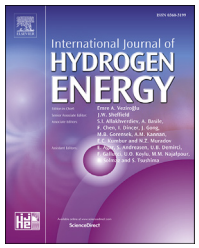

Accelerated fuel cell tests of anodic Pt/Ru catalyst via identical location TEM: New aspects of degradation behavior

K. Hengge [a], T. Gänsler [a], E. Pizzutilo [a], C. Heinzl [b], M. Beetz [c], K.J.J. Mayrhofer [a], C. Scheu [a,d,*,1]

[a] Max-Planck Institut für Eisenforschung GmbH, Max-Planck-Str. 1, 40237 Düsseldorf, Germany
[b] Elcore GmbH, Bayerwaldstr. 3, 81737 München, Germany
[c] Ludwig-Maximilians-Universität München, Butenandtstrasse 5–13, Haus F, 81377 München, Germany
[d] Materials Analytics, RWTH Aachen University, Kopernikusstr. 10, 52074 Aachen, Germany

ARTICLE INFO

Article history:
Received 30 June 2017
Received in revised form
4 August 2017
Accepted 17 August 2017
Available online 9 September 2017

Keywords:
Transmission electron microscopy
Electron tomography
Pt/Ru alloy
Identical location TEM
HT-PEMFC
Degradation

ABSTRACT

In the present work the stability, chemical composition and structure of a Pt/Ru catalyst alloy with a nominal ratio of 1/1 is investigated. The same catalyst particles are analyzed before and after potential cycling experiments using identical location transmission electron microscopy. The experiments were performed at room temperature at [0–1.0] V_{RHE} and [0–1.2] V_{RHE} to simulate conditions occurring during ramping up of fuel cells. With decreasing maximum potential value a higher stability is found. Dissolution and dealloying are identified to be the main degradation mechanisms during potential cycling with Ru being dissolved preferably. Also agglomeration and Ostwald ripening are taking place, the frequency decreasing the longer the experiment is performed. Advanced in-depth analysis of potential-dependent reshaping mechanisms are performed by calculating the three-dimensional volume of single particles both in the as-prepared state and after potential cycling experiments using electron tomography data. Evaluation of the volume-specific change of the accessible surface area of the catalyst helps to understand fuel cell performance deterioration.

Introduction

Catalyst design is an important aspect in the continuously growing field of fuel cell application [1]. Long-term stability and activity of the nanoparticles are considered to be among the key challenges to guarantee performance continuity over an extended lifetime. The most prevalent catalyst system for polymer-electrolyte-membrane fuel cells is based on platinum nanoparticles dispersed on a carbon support (Pt/C).

* *Corresponding author*. Max-Planck-Institut für Eisenforschung GmbH, Max-Planck-Straße 1, 40237 Düsseldorf, Germany.
E-mail addresses: k.hengge@mpie.de (K. Hengge), t.gaensler@mpie.de (T. Gänsler), pizzutilo@mpie.de (E. Pizzutilo), Christoph.Heinzl@elcore.com (C. Heinzl), michael.beetz@campus.lmu.de (M. Beetz), mayrhofer@mpie.de (K.J.J. Mayrhofer), scheu@mpie.de (C. Scheu).
[1] http://www.mpie.de/2902970/nanoanalytics_and_interfaces.
http://dx.doi.org/10.1016/j.ijhydene.2017.08.108

When applied as catalyst for a fuel cell anode, where the hydrogen oxidation reaction (HOR) occurs, different degradation mechanisms take place [2]. In the case of the catalyst support, carbon corrosion is frequently reported to occur [2–5]. A collapse of the basic framework of the carbon support results in a reduced porosity and hence mass transport limitations for the reactants. Macroscopically this can be seen in a diminishing fuel cell performance [6]. To circumvent corrosion, other support materials like metal oxides have been tested [7–11]. Not only the support material but also the highly dispersed catalyst nanoparticles are subject to diverse degradation mechanisms. The most frequently reported phenomena are particle dissolution, agglomeration, Ostwald ripening and particle detachment [2,12–17]. Particle dissolution is one of the main degradation mechanisms taking place during fuel cell operation [18,19]. On the atomic level, only atoms in the outermost surface shell can dissolve and their specific dissolution rate was found to be more or less independent of the particles' diameter [20]. However, since already in a 2 nm sized particle about 50% of the atoms are located in the outermost surface layer, smaller particles generally vanish faster than bigger ones [18]. The dissolved catalyst species can either leave the fuel cell in the water stream or redeposit at different locations of the fuel cell's electrode or membrane. Several studies report the presence of catalyst nanoparticles in the ionomer after fuel cell operation. These particles were redeposited by cross-leaking hydrogen [21–29]. Also, when the dissolved atoms redeposit on neighboring particles, Ostwald ripening is taking place. Small, energetically disfavored particles decrease in size while bigger particles grow further. The driving force of this process is the reduction of the surface energy since the fraction of atoms on the surface decreases with increasing particle size. The overall increase in particle size during fuel cell operation [30] can be also described by agglomeration. In this process, minimum two nanoparticles coalesce to form one bigger sized particle. The mechanism depends on the particles' distance and support properties. Hence, either previously separated particles actively move together [2] or a shrinkage of the carbon support as a result of corrosion [31] is taking place to meet this requirement. A further degradation mechanism, particle detachment, involves particles that detach from the carbon support as a whole. This can occur as a consequence of carbon corrosion. By use of a bimetallic catalyst, dealloying can take place additionally [32–36]. It is defined as selective dissolution of the less noble component when a certain potential threshold value is exceeded. Surface atoms dissolve first and as such expose underlying atoms of the second component. The result is an enrichment of the more noble metal on the surface of the particle. This can be either beneficial or harmful, depending on whether the metal composition on the particle's surface is important for the designated purpose of the catalyst. Meier et al. [2] reported that the degradation mechanisms depend on the metal-support interaction and the composition of the support but concluded that the weighting of these phenomena is not possible. To prove the occurrence of different particle degradation mechanisms and track changes of single particles, identical location transmission electron microscopy (IL-TEM) was employed [14,15]. TEM investigations and electrochemical tests are performed on the same location by using a TEM finder grid. The particles are studied in the as-prepared state and after an accelerated degradation protocol (ADP). The ADP typically consists of accelerated cyclic voltammetry (high scan rates) to simulate fuel cell start-stop operation in a standard three-compartment electrochemical cell [5]. Sequential TEM investigations of the previously measured, electrochemically altered catalyst reveal particle-specific degradation mechanisms [5,14,15].

The work in hand focusses on a high-surface-area carbon (HSAC) supported Pt/Ru based catalyst alloy which is applied as anode in high-temperature polymer-electrolyte-membrane fuel cells (HT-PEMFCs). The Pt/Ru system is the most frequently used alloy to enhance the carbon monoxide (CO) tolerance of Pt [37–42]. Depending on the overpotential applied, two mechanisms are proposed: At higher potentials water activation on Ru sites on the surface of the Pt/Ru based particle is taking place. A maximum activity was found when the Pt/Ru ratio was set to 1, as this is frequently reported to be the most active composition due to the maximum achievable number of Pt–Ru pairs on the particles' surface [39,40,43,44]. However other studies reveal a Pt/Ru ratio of 3/1 to exhibit the best CO tolerance [45]. At lower potentials Ru is reported to induce electronic changes on Pt. The reduced electron density in the Pt 5d band weakens the Pt–CO interaction (ligand effect) [40,45–48]. While pure Pt is known to adopt the face centered cubic (fcc) lattice, Ru crystallizes in the hexagonal close packed lattice (hcp) [49]. The crystal structure of the alloy is depending on the ratio of Pt/Ru used. According to Yamada et al. [50] an alloy exhibiting a Pt/Ru ratio of 1/1 will adopt the Pt fcc lattice, where half of the Pt sites in the crystal lattice are occupied by Ru atoms. When the Pt/Ru ratio is decreased to 1/2, the solubility limit of Ru in the Pt fcc phase is exceeded and concomitantly, both a Pt–Ru fcc phase and a Ru(-Pt) hcp phase are formed [50]. This explanation conforms to the Pt–Ru bulk phase diagram where a miscibility gap is present at higher Ru contents [51]. Besides Pt/Ru alloyed catalyst species, also Ru-core Pt-shell particles were in the focus of several research activities [42,52–55].

During regular fuel cell operation, the anode potential typically ranges from 0.0 V_{RHE} to a maximum of ca. 0.5 V_{RHE}. However, prior to operation, air can diffuse into the anode compartment resulting in a rise of the initial potential to an air open circuit voltage of ca. 1.0 V_{RHE} [56]. These conditions are applied in the present work to investigate the occurring degradation mechanisms during ramping up of the fuel cell, starting from room temperature. Moreover, during start-stop cycling, cell reversal can occur when a fuel cell stack is loaded but the anode is not supplied with enough fuel. In this case, the amount of current drawn from the fuel cell exceeds the amount that can be produced. As a result the anode potential increases up to values which are even more positive than the cathode potential and subsequently the cell voltage reverses [57–59]. According to Taniguchi et al. [57] several minutes in the cell reversal condition are sufficient to cause severe damage on the anode catalyst. Thereby, depending on the hydrogen stoichiometry supplied, the anode potential can vary in a wide range. Liang et al. [58] presented a study where

they progressively decrease the hydrogen stoichiometry from 1.09 to 0.55 and the resulting anode potential increased from 0.955 V to 2.058 V. In the present work 1.2 V_{RHE} is set as upper anode potential to study the influence of higher potentials on the Pt/Ru catalyst degradation.

The results presented are representative for the start-stop fuel cell operation procedure. The weighting for the different degradation mechanisms observed varies compared to continuous fuel cell operation where constant current densities and high temperatures are present. Still the obtained results can help to proceed with the targeted optimization of the Pt/Ru catalyst alloy and the development of a long-term stable catalyst to use in fuel cells.

Experimental details

Material

A layered carbon based support, consisting of a gas diffusion layer (GDL) at the bottom, a microporous layer (MPL) in the middle and a high surface area carbon on top (provided by elcomax GmbH) was impregnated with a mixture of the Pt and Ru precursors via an electroless deposition technique and subsequently thermally reduced. The so obtained catalyst layer (CL) on top was investigated in depth in the present work. The nominal Pt/Ru ratio was chosen to be close to 1. To conduct TEM and electrochemical analyses, the Pt/Ru loaded HSAC support was scratched off from the microporous layer and the gas diffusion layer with the help of a scalpel and ultrasonicated in 2-propanol/water (1:1) for 10 min.

Characterization methods

XRD

The crystal structure and lattice constants of the Pt/Ru catalyst were determined by X-ray diffraction. The measurement was performed with a Philips PW1830 diffractometer, equipped with a proportional counter detector, type PW 1711, and a cobalt X-ray source ($\lambda = 1.79$ Å). The 2θ detection range was set between 10° and 130°. The XRD data were acquired in a continuous mode by using a step size of $2\theta = 0.02°$ and a count time of 25 s per step. A power setup of 40 kV/30 mA and a rotation speed of 1 loop/s were used.

TEM

Transmission electron microscopy and related techniques were performed to study the structural degradation behavior of the Pt/Ru catalyst on the sub-nanometer scale. For TEM sample preparation the previously prepared suspension (see Materials section) was diluted and dropcasted onto a lacey carbon film coated gold finder grid (NH7 from Plano). The finder grids used exhibit small letters with defined distances between them, thus enabling the TEM user to find pre-investigated areas again. TEM measurements were done on an FEI 60–300 Titan Themis which was operated at 300 kV, a JEOL JEM-2200FS and a Phillips CM20 both operated at 200 kV. The Titan Themis is equipped with a C_s-corrector for the condensor system. For STEM imaging the attached high-angle annular dark-field (HAADF), ADF and bright-field (BF) detectors were used. The convergence angle was 23.8 mrad, the collection angle 73–352 mrad (HAADF) and the spot size was about 1.5 Å. Quantitative EDX analysis was performed using the attached Super X-EDX detector from Bruker and the Bruker software Esprit 1.9.4.3348. Electron diffraction experiments were carried out on the JEOL TEM and the CM20.

Electron tomography

The 3D spatial arrangement of the Pt/Ru catalyst and their volume as well as surface area were analyzed via electron tomography. Tilt series were acquired in the Titan Themis using a dedicated single-tilt tomography holder from FEI. Tilt angles were chosen in the range of ±60° with tilt increments of 10°. The reconstruction of the 3D volume was performed by use of the simultaneous iterative reconstruction technique (SIRT) [60–62] and refined by the discrete algebraic reconstruction technique (DART) [63,64].

Cyclic voltammetry

A non compact three-electrode teflon electrochemical cell [13] is used to perform the electrochemical measurements. The counter electrode and reference electrode, a graphite rod and a commercial Ag/AgCl electrode (Metrohm) are housed in separate compartments. Furthermore, the reference electrode is separated by a Nafion membrane (Tschurl modification) to prevent any chloride contamination of the electrolyte. The working electrode is a glassy carbon disk embedded in a teflon rotating disk electrode tip that can be mounted on a commercial rotating shaft (Radiometer Analytical, France). For the IL-TEM measurement the prepared TEM finder grid is placed on top of the glassy carbon rotating disk electrode tip. Two different accelerated degradation protocols (ADPs) were used in this study:

- ADP-1.0: cyclic voltammetry [0–1.0] V_{RHE}, 200 mV s^{-1}, H_2 saturated $HClO_4$, room temperature, no rotation;
- ADP-1.2: cyclic voltammetry [0–1.2] V_{RHE}, 200 mV s^{-1}, H_2 saturated $HClO_4$, room temperature, no rotation;

The ADPs were stopped after regular intervals of cycles (ADP-1.0 after 5000, 15000 and 25000 cycles, whereas ADP-1.2 after 2000 and 7000 cycles) to perform IL-TEM analysis at different degradation stages. In the case of ADP-1.0 a separate measurement is added in order to monitor the evolution of the electrochemical surface area. In this case the catalyst ink is directly dropcasted (20 μL) onto the glassy carbon electrode; after drying the homogeneity of the film is verified. The electrochemical surface area (ECSA) is then evaluated with the CO-stripping method (after 1, 100, 200, 500, 1000, 5000, 15000, 25000 of ADP-1.0) and the charge underlying the CO-stripping peak is calculated. A charge density of 195 μC cm^{-2} is assumed for evaluating the Pt surface area. Further information about the CO-stripping method can be found in literature [65]. All electrochemical parameter, as well the potentiostat (Gamry reference 600), the gas system and the rotator are controlled through an in-house-developed LabVIEW based software. The electrolyte is 0.1 M $HClO_4$, prepared from concentrated $HClO_4$ (Merck, Suprapur) and ultrapure water (UPW, 18 MΩ, Millipore).

Results and discussion

Structure and composition of an as-prepared Pt/Ru catalyst

An overview TEM micrograph of a representative sample area is displayed in Fig. 1a. The spherical particles are the HSAC support material with a diameter in the range of 50–100 nm. Each particle exhibits the characteristic structure of turbostratic carbon as visible in the high resolution (HR) TEM micrograph (Fig. 1b) with nearly parallel (0001) planes possessing a distance of 4.90 ± 0.08 Å. On the surface of the carbon support, the Pt/Ru catalyst is located. It can be recognized by its dark contrast in the bright field TEM images which is mainly due to diffraction and the high atomic mass of Pt and Ru. Electron diffraction analysis reveals circular diffraction patterns consisting of many individual spots, thus indicating the presence of several Pt/Ru catalyst nanoparticles (Fig. 1). Distinct features are visible: diffuse rings due to the turbostratic carbon support and diffraction spots lying on rings. A detailed discussion of the results of the diffraction analysis, including crystal structure and lattice distortion, is presented below. To take advantage of the difference in the atomic weight of Pt and Ru compared to the carbon based support material, HAADF STEM images were taken where the intensity is roughly proportional to the square of the atomic number of the elements. In Fig. 1c an overview HAADF STEM micrograph is presented, showing bright appearing catalyst nanoparticles on the dark appearing HSAC support. The black regions are vacuum. Generally two different shapes of the Pt/Ru catalyst can be found: spherical catalyst nanoparticles and bigger sized morphologies of polycrystalline chains which are formed by interconnected catalyst nanoparticles. The size of the individual, spherical NPs is in the range of 1.21 ± 0.36 nm. Several interconnected, monocrystalline nanoparticles, forming a bigger sized chain, are displayed in Fig. 1d. The chains reveal on average a width of 2.1 ± 0.4 nm, the overall length is varying in a broad range from ca. 10–30 nm.

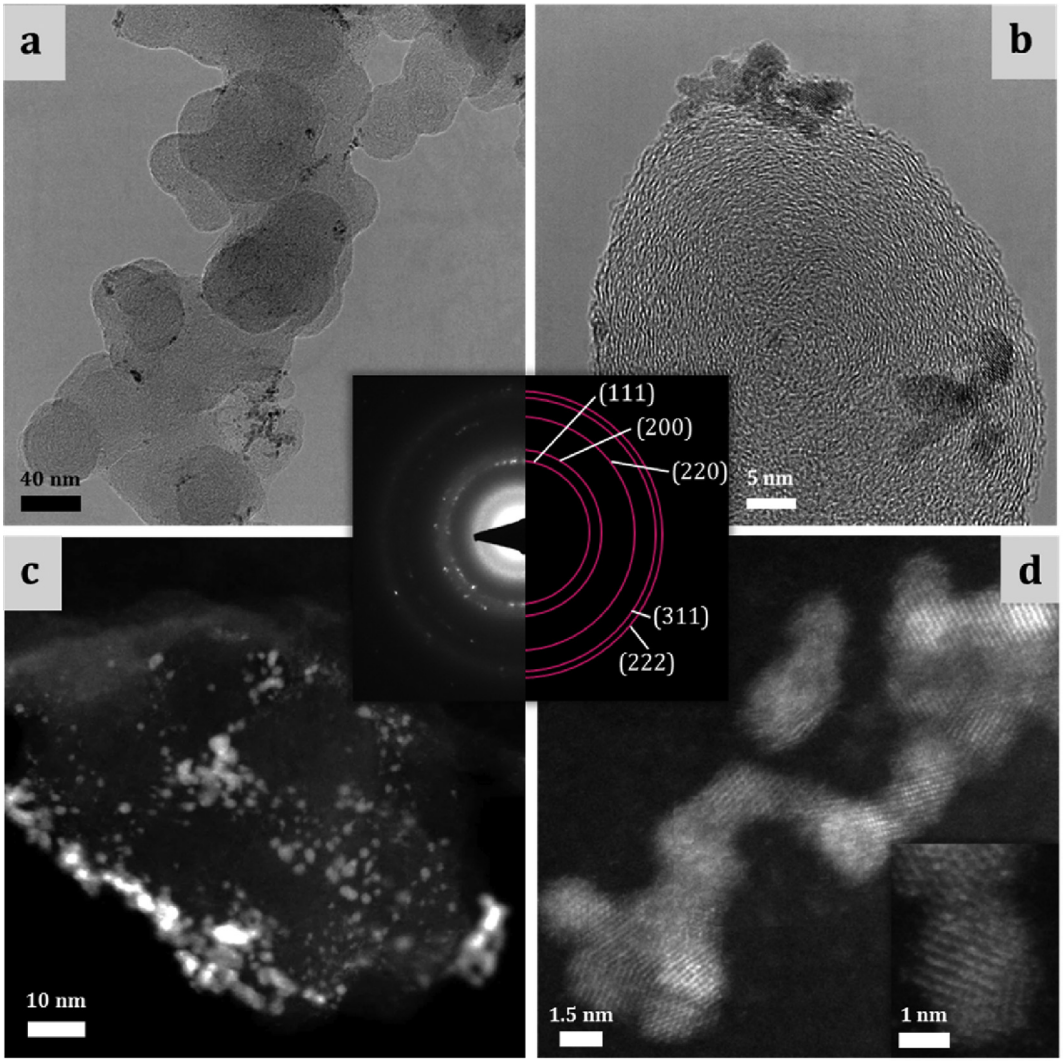

Fig. 1 – TEM and STEM micrographs of Pt/Ru catalyst nanoparticles on their HSAC support in the anode catalyst layer: a) TEM overview micrograph reveals several spheres of the catalyst loaded HSAC support; b) HRTEM image exhibits characteristic structure of turbostratic carbon and the dark features are the catalyst particles; c) HAADF STEM overview micrograph where the bright areas are the Pt/Ru catalyst; d) polycrystalline chain of grown-together catalyst nanoparticles.

EDX measurements were performed in STEM mode on a variety of individual Pt/Ru catalyst nanoparticles, bigger sized chains and large areas exhibiting a size of 100 nm × 100 nm and more. Although a Pt/Ru precursor ratio of 1 was used, the actual composition of the catalyst was found to vary in a broad range. When all EDX measurements are taken together, the lowest amount of Ru in a single particle was found to be 14.8 atom% while the largest amount was 87.9 atom%. The amount of Pt is vice versa. Fig. 2 displays two representative EDX maps exhibiting the elemental distribution of Pt and Ru in single nanoparticles (Fig. 2a) and in a bigger sized catalyst morphology (Fig. 2b). The numbers give the Pt/Ru ratio of the different regions. The data show that it is not possible to predict the elemental composition of single particles solely by visual interpretation of the HAADF STEM micrographs.

The crystal structure of the nanoparticles was determined by three complementary methods: Electron diffraction experiments were carried out by use of a selected area diffraction aperture (size ca. 200 nm) to obtain information on the crystallinity of several Pt/Ru catalyst nanoparticles. Additionally, high-resolution (HR) TEM measurements were performed to investigate the crystal structure of single Pt/Ru alloyed NPs by calculating their Fourier transform. The crystallinity of a millimeter sized sample area was analyzed by XRD measurements.

An exemplary electron diffraction pattern of several Pt/Ru catalyst NPs exhibiting different shapes and elemental composition is displayed in the inset in Fig. 1. It reveals the presence of an fcc lattice even though the d-spacings measured are on average 1%–2% smaller than literature values of Pt [49]. This can be explained by the smaller atomic radius of Ru which, in the alloy, substitutes some of the Pt atoms in the fcc lattice. Analysis of HRTEM micrographs also reveals solely the presence of the fcc lattice. Single particles were investigated by measuring the distance and the angle between their lattice planes in the Fourier transform.

Fig. 3 presents the XRD pattern of the Pt/Ru electrocatalyst in the as-prepared anode of a high-temperature polymer-electrolyte-membrane fuel cell (HT PEMFC). The diffraction

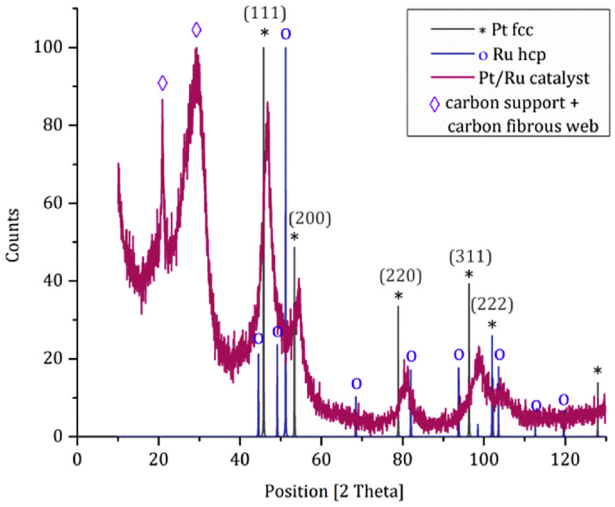

Fig. 3 – Result of the XRD measurement of the investigated Pt/Ru catalyst (purple) in comparison to literature values of polycrystalline Pt (*) and Ru (o) [49]. The shift of the diffraction peaks measured toward higher angles indicates the formation of an fcc Pt/Ru alloy with smaller lattice constants than fcc Pt. (For interpretation of the references to colour in this figure legend, the reader is referred to the web version of this article).

peak at 20.9° corresponds to the turbostratic HSAC material (d = 4.90 ± 0.08 Å) used as catalyst support and the one at 29.3° is stemming from the carbon fibrous web (d = 3.54 ± 2.47 Å) which is the gas diffusion layer. Apart from these two, the other diffraction peaks originate from the Pt/Ru electrocatalyst. The grey and blue lines correspond to the positions of the peaks of pure Pt in fcc modification (a = 3.9231 Å [49], marked with *) and Ru in hcp modification (a = 2.7039 Å, c = 4.2817 Å [49], marked with o). The Pt/Ru diffractogram resembles all the reflections from the Pt fcc lattice. However, analogous to the electron diffraction analysis, there is a clear shift toward higher angles observed. This can be explained by

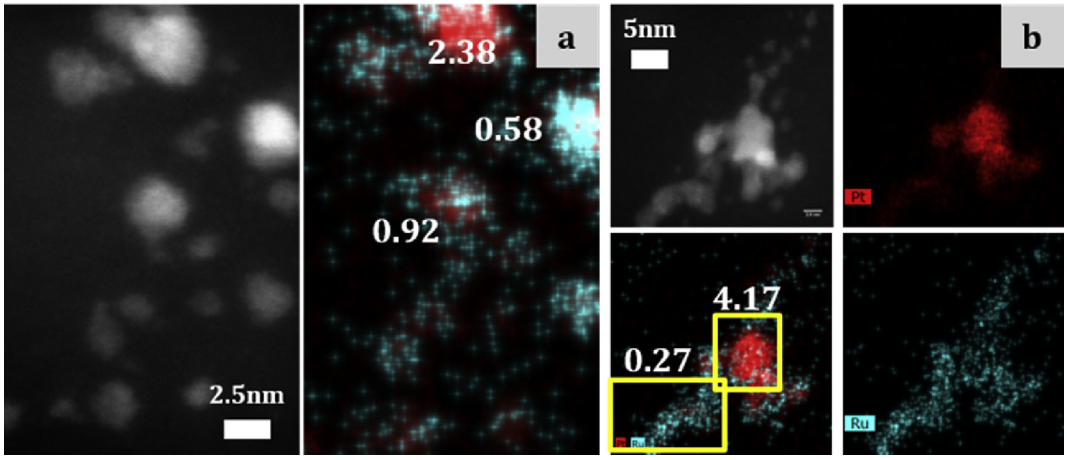

Fig. 2 – EDX maps reveal the elemental distribution of Pt (red) and Ru (blue) in a) single nanoparticles; b) bigger sized network of chains of interconnected nanoparticles. (For interpretation of the references to colour in this figure legend, the reader is referred to the web version of this article).

the substitution of the smaller Ru atoms on the Pt fcc lattice sites and the subsequent formation of a Pt/Ru fcc alloy. The lattice parameter of this alloy was calculated to be 3.91 ± 0.01 Å. Hence the lattice distortion in the investigated Pt/Ru electrocatalyst compared to the pure Pt fcc lattice is about 0.31%. The average crystallite size in the millimeter sized area measured was calculated to be 2.11 nm.

Additional peaks, indicating the presence of the Ru hcp phase, are not visible in the Pt/Ru diffractogram. Even though this is no proof for the absence of a Ru hcp phase in the sample, the amount would be below the detection limit.

To summarize, EDX measurements revealed local Ru contents of up to 87.9 atom% where the Pt/Ru bulk phase diagram would predict the hcp lattice [51]. However, electron diffraction patterns, HRTEM investigations and XRD measurements reveal that the investigated Pt/Ru catalyst particles solely adopt the fcc lattice but exhibit a slightly smaller lattice constant than the pure Pt fcc lattice. These results conform to the work of Yamada et al. [50]. The authors studied Pt/Ru catalysts exhibiting a 1/1 ratio and solely found the presence of the fcc lattice. However when they decreased the atomic ratio to 1/2, the solubility limit of Ru in the Pt fcc phase was exceeded and a small amount of the Ru hcp phase was present in their sample.

To obtain information whether different chains of catalyst nanoparticles are connected and to address the accessibility of the surface in the bigger Pt/Ru catalyst networks for the gaseous H_2, electron tomography experiments were performed (see below). Even though in the final reconstruction it is not possible any more to distinguish between single nanoparticles due to limited resolution, the chains that are formed by them can be studied. From the 3D reconstructed catalyst morphologies, the surface area and volume can be calculated and thereby the influence of the potential cycling can be quantified. In none of the reconstructed 3D volumes of Pt/Ru catalyst networks it is possible to distinguish between Pt and Ru. However pure Pt and pure Ru should in principle be distinguishable solely by their contrast in the HAADF STEM micrographs. Therefore the result indicates that the two elements formed Pt/Ru alloys in accordance to the EDX analysis.

Degradation under HOR at the ramp-up procedure

Structural changes

During ramping up of the fuel cell, air can be present in the anode leading to an initial open circuit voltage of ca. 1.0 V_{RHE}. The influence of these high potentials on the anode catalyst is studied in the following. Similar to fuel cell ramping up conditions, the measurements were carried out at room temperature. To track small changes and intermediate steps of catalyst degradation, electrochemical cycling experiments were performed in the potential range between [0–1.0] V_{RHE}. Two characteristic sample areas were studied in detail: single Pt/Ru agglomerates formed by chains of catalyst nanoparticles and overview areas exhibiting both single, spherical nanoparticles and bigger morphologies. A HAADF STEM micrograph of an as-prepared larger sample region is displayed in Fig. 4a while Fig. 4b–d are taken after 5000, 15000 and 25000 cycles in the potential range [0–1.0] V_{RHE}. A single Pt/Ru electrocatalyst network on its carbon support is displayed before simulating fuel cell operation (Fig. 4e) as well as after 5000 (Fig. 4f), 15000 (Fig. 4g) and 25000 (Fig. 4h) cycles. Clearly, after each series of cyclic voltammetry, the Pt/Ru catalyst has altered.

The as-prepared anode (Fig. 4a) exhibits a variety of small and bigger particles which are more or less equally distributed on their support. Additionally bigger agglomerates are present. After each series of potential cycling, the structure of the investigated area changed. The overall degradation effect is strongest after the first 5000 cycles and the smaller particles are more prone to degradation than the bigger ones. Two explanations are likely to be the reason for this observation: initial degradation due to severe dissolution of the smallest nanoparticles [18] and coalescence of particles which are in close vicinity [13]. Both mechanisms are thermodynamically driven in order to reduce the surface/volume ratio of the catalyst. Five characteristic areas highlighting different degradation mechanisms that occur during the electrochemical cycling are marked in Fig. 4a–d. The green circle (1) emphasizes a particle that gradually dissolves during the electrochemical treatment. The shrinkage in diameter can nicely be seen in the first 15000 cycles and after an overall number of 25000 cycles the particle dissolved almost completely. The blue circle (2) highlights a bigger catalyst particle which is surrounded by small nanoparticles in the as-prepared state. All of these small particles vanished after the first interval of potential cycling and either dissolved and redeposited or migrated on the surface of the carbon support to the bigger particle close by [13]. The elongated, bigger sized particle changes its shape during the electrochemical treatment to become almost spherical after 25000 cycles. This reshaping process is thermodynamically driven as well. The third example is marked by 3 (yellow circle). Here two particles are located on the carbon support exhibiting a distance of ca. 3 nm between them. Potential cycling causes these nanoparticles to migrate in direction of each other, to form a bridge after 15000 cycles and finally, after 25000 cycles, to agglomerate. The circle numbered 4 (pink circle) presents an area where several degradation mechanisms are taking place in sequence. In the first 5000 cycles, four distinct nanoparticles exhibiting a similar diameter were formed out of differently shaped particles from the as-prepared state. After 15000 potential cycles, the upper two particles agglomerated, thus forming one bigger spherical particle. With ongoing potential cycling, the nanoparticle in the middle decreases in size due to dissolution. Supposedly further cycling would cause this particle to dissolve completely. The fifth and last example highlights a collection of 11 differently sized particles on the carbon support (labelled with 5). Electrochemical cycling causes distinct changes: coalescence of the uppermost three particles and dissolution of the five smallest particles while the three bigger sized particles on the lower right side stay visually unchanged.

These five different examples show that there are always several degradation mechanisms taking place simultaneously during the potential cycling experiment. However, assigning certain changes to a specific degradation mechanism can be ambiguous. For example, when a nanoparticle is missing after previously performed potential cycling, it could have either dissolved, moved to another particle close by or detached.

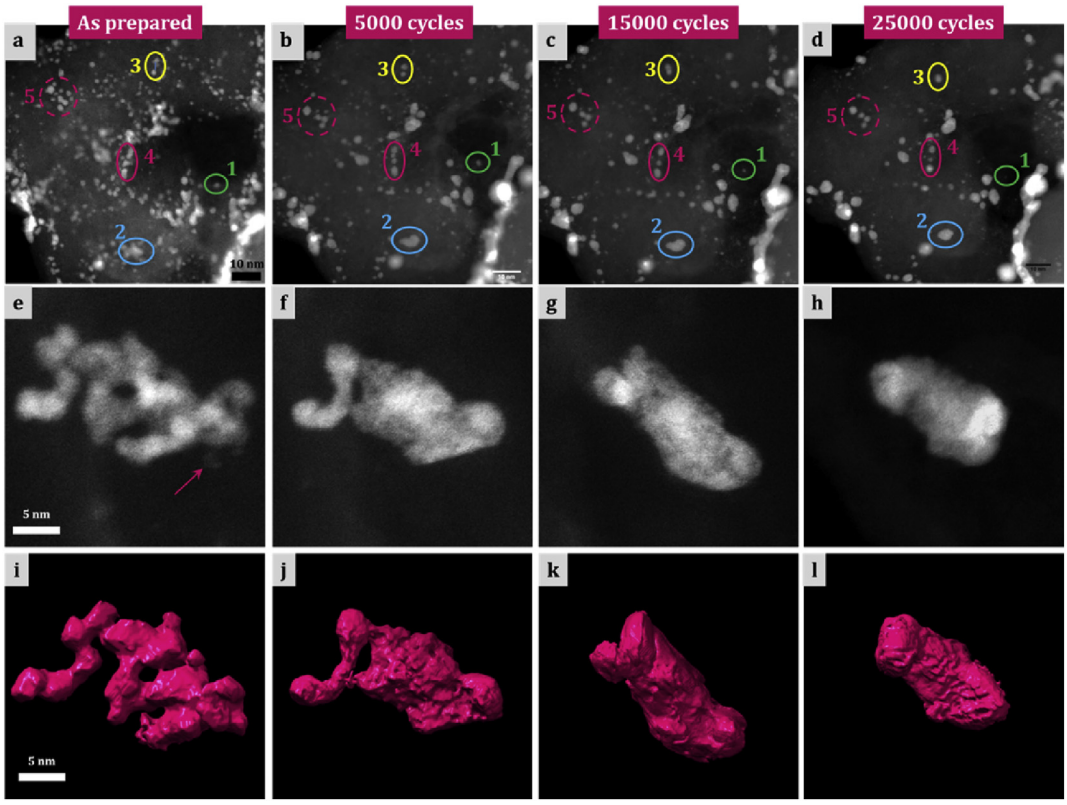

Fig. 4 – HAADF STEM micrographs of an overview area (a–d) and a bigger sized Pt/Ru catalyst morphology (e–h) a), e) The images show the as-prepared state; b), f) after 5000 cycles; c), g) after 15000 cycles; d), h) after 25000 cycles in the potential range [0–1.0] V_{RHE}; i) – l) display the reconstructed volume obtained by electron tomography.

However, when taking the particle's environment into account, the possibility for one or another degradation mechanism changes. For this reason the mechanisms described above are the most likely ones to occur. Also the intensity of the degradation processes can vary. Dissolution is the obvious example: while the greatest part of the catalyst particles dissolved after the first 5000 cycles there are still some areas left where gradual dissolution can be observed (see circle marked with 1 in Fig. 4a–d). A variety of parameters are conceivable to affect the severity of the resulting degradation mechanisms on single particles: major roles play, apart from composition, also the metal-carbon interaction, the constitution of the carbon support, the wetting of the catalyst's surface with the hypochloric acid used as electrolyte and the conductivity between the catalyst morphology and the electrodes of the electrochemical cell. Unfortunately these parameters are not quantifiable.

The particle size distribution diagram in Fig. 5 visualizes changes of the catalyst nanoparticles' dimensions in the area displayed in Fig. 4a–d. In the as-prepared sample the diameter of the catalyst particles is on average 1.21 ± 0.36 nm. After 5000 potential cycles, the mean particle size was found to increase (1.57 ± 0.68 nm) and also the size distribution range of the catalyst particles broadened. Additionally a tail towards bigger particle sizes becomes apparent in the log-normal particle size distribution. Both trends, particle growth and an increasing spread in the particle size distribution, intensify with ongoing potential cycling. After 15000 cycles, the mean size of the particles was found to be in the range of 1.64 ± 0.71 nm and increasing to 1.73 ± 0.61 nm after 25000 cycles. A tail towards bigger particle sizes in a log-normal particle size distribution diagram is an indication of agglomeration taking place. A tail towards smaller particle sizes would be a hint for Ostwald ripening.

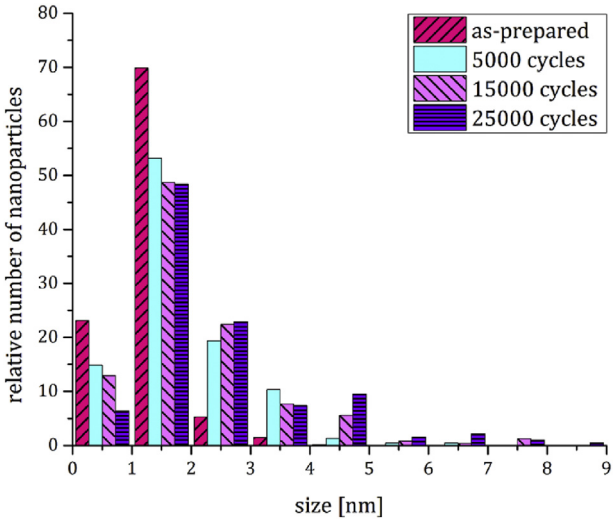

Fig. 5 – Particle size distribution in the overview area presented in Fig. 4a–d. With increasing potential cycling time, a tail towards bigger particle sizes becomes apparent.

After 5000 cycles, the greatest part of the particles dissolved or agglomerated and simultaneously the average distance between particles increased. In this state agglomeration becomes less likely and dissolution remains as the main and most likely degradation mechanism. However, after each potential cycling interval there are still small NPs in the nanometer scale range left on the HSAC support. Interestingly the greatest part of these particles stays on their location and does neither dissolve nor grow in size. A possible reason could either be that these NPs are sheltered by surrounding carbon material (and would no longer be electrochemically active) or that the metal-carbon interaction in these areas is big enough to keep the particles in place.

EDX measurements were performed to study the chemical composition of the nanoparticles before and after the electrochemical cycling. The change of the ratio of Ru and Pt is measured. From previous studies and literature research it is known that during FC operation Ru is more prone to dissolution than Pt [29,66]. This is as well the case in the investigated sample. The observed dealloying effect is caused by a faster dissolution of the less noble metal, which is Ru. In the case of the bimetallic Pt/Cu system, the formation of a core-shell structure is reported [35,36]. However, this is not the case for the investigated Pt/Ru catalyst. Rather an irregular distribution of the two components within single catalyst morphologies is observed. The average chemical composition in the initial state is designed to be 1/1. This has been proven by EDX measurements on other overview areas but not specifically on the location presented in Fig. 4a. In the case of the as-prepared state, the data given in Table 1 are nominal values. After each series of electrochemical cycling, the Pt/Ru ratio increased, thus indicating that Ru slowly is leaching out of the alloy. After 5000 cycles the Pt/Ru ratio is 1.22, after 15000 cycles 1.28 and after 25000 cycles 1.82 (Table 1). These results stem from overview EDX measurements of the continuously altering area as displayed in Fig. 4a–d. After 25000 cycles the Ru content in different particles ranges between 30 and 50 atom%.

Additional to overview areas, individual, bigger sized Pt/Ru catalyst networks exhibiting a high Ru content were analyzed at higher magnification before and after potential cycling between [0–1.0] V_{RHE}. A representative example is displayed in Fig. 4e–h. The results of the corresponding electron tomography are shown in Fig. 4i–l before and after 5000, 15000 and 25000 cycles. Additionally a movie in gif-format, where the reconstructed particles are rotated, is provided in the supplementary. Here, but also in the other Pt/Ru catalyst structures, particle growth was found to be the main degradation mechanism. This could be either due to agglomeration of particles or due to Ostwald ripening as discussed above. Since the individual particles are in close vicinity and/or connected to each other, thus forming the bigger sized network, the catalyst material is supposed to diffuse and grow together during potential cycling. Concomitant with this reshaping process is the minimization of the surface area of the morphology. This process is thermodynamically driven. Additionally there are also individual nanoparticles located in the vicinity of the catalyst morphology as displayed in Fig. 4e and highlighted by an arrow. These nanoparticles vanished after the first 5000 cycles. Presumably they either moved towards the bigger catalyst morphology close by and grew together or dissolved and redeposited on it.

Of the 3D reconstructed Pt/Ru catalyst particle, the change of volume and corresponding accessible surface area was calculated and summarized in Table 2. The as-prepared catalyst morphology exhibits a volume of 577 nm^3 with an accessible surface area of 917 nm^2, resulting in a surface/volume ratio of 1.6 nm^2/nm^3. After 5000 cycles, the volume of the investigated Pt/Ru catalyst network stayed more or less constant ($V = 567\ nm^3$), however the surface area decreased ($A = 725\ nm^2$) and so did the surface/volume ratio (1.3 nm^2/nm^3). The rapid decay of the extent of the accessible surface area can be explained by the collapse of the lower part of the network and the concomitant formation of a compact particle. This degradation process can mainly be attributed to agglomeration. After 15000 cycles, the volume of the investigated particle was found to increase ($V = 655\ nm^3$) while the accessible surface area further decreased to 663 nm^2. Compared to the state after 5000 cycles the related surface/volume ratio further decreased to 1.0 nm^2/nm^3. An explanation for this could be that during the second potential cycling interval, Ostwald ripening was taking place preferably. The additional atoms stemming from the surrounding increased the particle's volume while they scarcely influence the extent of the particle's surface. However, simultaneously occurring agglomeration results in a lower surface area. After 25000 cycles both volume and surface area of the catalyst further decreased due to dissolution taking place preferably ($V = 602\ nm^3$ and $A = 621\ nm^2$). The surface/volume ratio stayed constant and the whole particle was becoming more compact. Supposedly when the potential cycling experiment would be continued, the investigated catalyst particle would adopt a spherical shape which is thermodynamically preferred. To get an idea of the fineness of the reconstruction that was performed, every second micrograph of the tilt series in the tilt range of ±60° obtained from the particle presented in

Table 1 – Elemental composition of the overview area presented in Fig. 4a–d. Please note that the initial composition of the as-prepared state is designed to be 1 and was not specifically measured at this location.

	as prepared	5000 cycles	15000 cycles	25000 cycles
Ru [atom%]	50	45.1	43.8	35.6
Pt [atom%]	50	54.9	56.2	64.4
Pt/Ru	1	1.22	1.28	1.82

Table 2 – Elemental composition of the Pt/Ru catalyst network presented in Fig. 4e–h and volume and surface area of the reconstructed catalyst network presented in Fig. 4i–l.

	as-prepared	5000 cycles	15000 cycles	25000 cycles
Ru [atom%]	74.7	64.8	61.3	57.1
Pt [atom%]	25.3	35.2	38.7	42.9
Pt/Ru	0.34	0.54	0.63	0.75
Volume [nm^3]	577	568	655	602
Surface area [nm^2]	917	725	663	621
Surface/Volume [nm^2/nm^3]	1.6	1.3	1.0	1.0

Fig. 4e is given in supplementary Fig. S1. The images are compared to the DART reconstruction and the resulting 3D volume. The intensity distribution obtained from the DART reconstruction is very similar to the HAADF STEM micrographs for all tilt angles indicating a good reliability of the data extracted from the reconstruction.

EDX measurements were carried out in STEM mode and elemental distribution maps were obtained from the network displayed in Fig. 4e–h. Quantification of Pt and Ru revealed an increasing Pt/Ru ratio with an increasing number of potential cycles (Table 2). Starting with a Pt/Ru ratio of 0.34 in the as-prepared sample, the ratio increased to 0.54 after 5000 cycles, 0.63 after 15000 cycles and 0.75 after 25000 cycles. The distribution of both elements is non-uniform within the catalyst network. Locally changing Ru contents between 55.8 atom% in the chain on the left side, up to 83.4 atom% on the right side are present in the as-prepared morphology. After 25000 potential cycles, the left side of the catalyst is composed of 38.1 atom% Ru while its right side contains up to 65.5 atom% Ru.

Electrochemical surface area evolution

The evolution of the electrochemical surface area is monitored with the CO-stripping technique under ADP-1.0. Cyclic voltammetry in the potential range of [0–1.0] V_{RHE} at 200 mV s^{-1} in 0.1 M perchloric acid is interrupted to perform CO stripping experiments after deliberately chosen intervals of 100, 200, 500, 1000, 5000, 15000 and 25000 cycles (Fig. 6). Additionally, the accessible surface area of Pt in the investigated Pt/Ru alloy was calculated from the CO-stripping voltammogram (see inset in Fig. 6).

In the as-prepared initial state, the adsorbed monolayer of CO is removed from the Pt active sites at a potential of ∿0.65 V_{RHE}. This value is in the order of 0.2 V_{RHE} lower compared to pure Pt/C nanoparticles with a mean diameter of ca. 3 nm (∿0.83 V_{RHE}, see supplementary Fig. S2). As mentioned before,

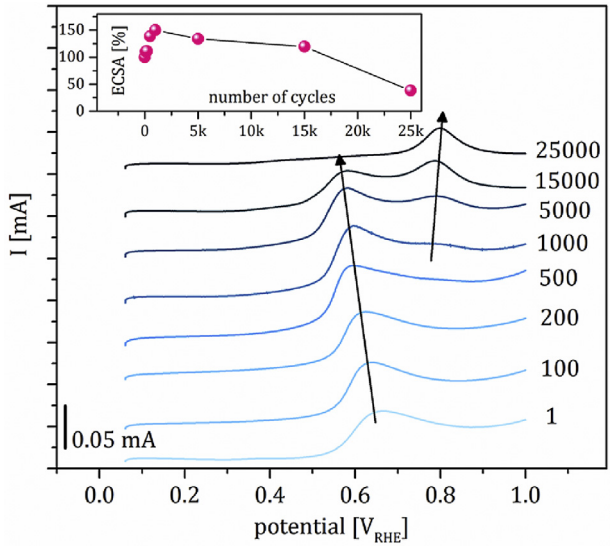

Fig. 6 – CO-stripping voltammogram evolution at different stages of the ADP-1.0 ([0–1.0] V_{RHE}). From the integrated peak the percentage evolution of the accessible surface of Pt is calculated (inset).

Ru was added to enhance the CO tolerance of the Pt catalyst. This purpose was achieved: in the presence of Ru, CO oxidized from the surface of Pt more easily which explains the observed shift of the stripping towards lower potential. Similar observations illustrating the improved CO tolerance of a Pt/Ru catalyst alloy compared to pure Pt were reported by Gasteiger et al. [43]. In the present work, the CO-stripping voltammograms at different stages of the degradation experiment, display the following two trends: i) a shift in the first peak position towards lower potential values down to 0.58 V_{RHE} and ii) after 500 cycles the gradual formation of a second peak at higher potentials in the range of 0.77–0.8 V_{RHE}. The exact values after each potential cycling interval are listed in Table S1 in the supplementary information. As mentioned above, the observed shift of the first peak towards lower potentials indicates a more efficient removal of CO from the Pt surface in the Pt/Ru catalyst system. However, the appearance of the second peak implies that there is another contribution which removes the beneficial effect of Ru. Additionally the contribution of the first peak is decreasing with the catalyst degradation until it vanishes after 25000 cycles. Supposedly this is related to the change in surface composition as Ru is dissolving at a faster rate than Pt (this implies that there could be a threshold value of Ru to enhance the CO tolerance of Pt) and to the contribution of smaller particle being formed as a consequence of dissolution. However, a detailed interpretation is difficult as these changes are due to the superposition of several degradation mechanisms occurring in parallel.

The percentage evolution of the surface area of Pt (from the initial 0.37 cm^2) under ADP-1.0 was calculated from the CO-stripping charge, assuming a charge density of 195 μC cm^{-2} and is summarized in supplementary Table S.1. Interestingly, during the initial cycles, a large increase of ca. 50% of the accessible surface area of Pt (up to 0.55 cm^2 after 1000 cycles compared to the as-prepared state) is observed. Afterwards the surface area is decreasing gradually down to 0.14 cm^2 after 25000 cycles. An increasing surface area can be explained either by a decreasing particle size or by an increase of the available Pt surface area. Baldizzone et al. [67] observed a similar increase of the ECSA of their Pt/Ni catalyst when starting their potential cycling experiment. The authors found that dealloying led to the formation of a porous catalyst structure, thus increasing the accessible surface area. However, in the work in hand no formation of porous structures was observed. Rather it is supposed that excess Ru is initially blocking catalytically active sites of Pt on the surface of the alloyed particles. Also the presence of a small amount of Ru-oxides and hydroxides on the Pt/Ru alloy is reported in literature to lower the performance [45,46,50,68]. It is also known, that Ru oxides and hydroxides are less stable than fcc Pt/Ru solid solutions [66,69]. Generally, since Ru is dissolved preferably (dealloyed), especially in the first 1000 cycles subjacent Pt is exposed and can be detected with CO-stripping. Thus, dealloying of surface Ru explains the increase in the accessible surface area of Pt as was also observed for a dealloyed Pt/Ni catalyst [33]. Similar observations were made in the fuel cell stack where the full performance of the cell is only achieved after a certain conditioning phase [29].

As mentioned above, the described CO stripping measurements were performed in the potential range of [0–1.0]

V_{RHE}. For comparison, the overview area and the individual Pt/Ru catalyst particle network displayed in Fig. 4 were investigated after 5000, 15000 and 25000 cycles in the same potential interval. In the cyclic voltammetry experiment, the overall ECSA of the catalyst increases in the first 1000 cycles by ca. 50% and decreases after 5000 cycles gradually while the most significant drop is recorded after 25000 cycles. However up until 15000 cycles, the extent of the accessible surface area of Pt measured is higher than in the as-prepared, initial state. This seems to contradict STEM observations. In the overview area in Fig. 4a–d dissolution and particle growth are taking place from the start. Both mechanisms result in a constantly decreasing accessible surface area of the catalyst. To explain the difference, a simple model can be used. Assuming an entirely alloyed Pt/Ru catalyst particle, both elements would be distributed homogeneously in the entire volume. That would as well imply that the surface of the particle would be composed of 50% Pt atoms and 50% Ru atoms. Consequently, since CO adsorbs to Pt atoms, the measurable surface area of Pt would correspond to half of the total surface area present. With ongoing potential cycling a preferred dissolution of the less noble Ru is recorded. Since the surface atoms dissolve first, the underlying Pt atoms are exposed thus increasing the measurable surface area of Pt. This effect is dominating in the first 1000 potential cycles and thus the available surface area of Pt is increasing. With ongoing potential cycling, other degradation mechanisms like agglomeration and particle coarsening gain influence and the Pt surface area is decreasing. Additionally, with ongoing dissolution of Ru, the CO tolerance of Pt is decreasing. The water activation and electronic effect of Ru on Pt are only present when both Ru and Pt are in close vicinity [32,43,44,68]. The loss of this feature is the reason for the appearance of the second peak that forms during the CO stripping experiment at higher potential values. In fact, the overall amount of Ru after 25000 cycles is still considerably high: 36 atom% of previously 50 atom% are preserved. However, if the greatest part of the element is only present in the bulk of the particles and not on the surface, the measurable electrochemical behavior of the Pt/Ru alloy differs markedly. Cyclic voltammetry and CO stripping as well as catalysis are surface sensitive mechanisms. EDX measurements on the other hand reveal the elemental composition of the overall 3D volume of particles. However, in case dissolution of Ru atoms at the surface of the catalyst particles is taking place, the resulting Pt-rich outer shell is either not continuous or so small in thickness that it was not detected by EDX measurements in STEM mode. Still the simple estimation allows combining all observations made from STEM and electrochemical analysis and completing the picture of nanometer and subnanometer scale degradation processes that are responsible for changing CO tolerance mechanisms during the electrochemical treatment: A depletion of Ru on the surface of Pt/Ru catalyst particles and subsequently a reduced CO tolerance of the overall system.

Degradation under cell reversal conditions

To study the influence of the Pt/Ru catalyst degradation behavior on the upper potential during start-stop cycling, a second cyclic voltammetry experiment was carried out in the interval range of [0–1.2] V_{RHE} (Fig. 7). Volume and accessible surface area of the investigated particle in the as-prepared state and after 2000 and 7000 cycles were calculated from the electron tomography data and are summarized in Table 3. A video in gif-format showing the reconstructed 3D volumes of the investigated particle is presented online in the supplementary. In the reconstruction, the as-prepared catalyst was found to exhibit a volume of 3770 nm^3 and a surface area of 5247 nm^2. In the first interval of the electrochemical cycling experiment (2000 CVs), the morphology of the Pt/Ru catalyst particles altered only in the nanometer scale range and volume and accessible surface area slightly decreased ($V = 3706\ nm^3$ and $A = 4427\ nm^2$). This is due to agglomeration or Ostwald ripening that balance dissolution. However, the shape of the overall morphology of the Pt/Ru catalyst is preserved. This is not the case after the second interval of the cyclic voltammetry experiment of 7000 cycles. The greatest part of the Pt/Ru particle has dissolved and only five larger nanoparticles are observed. The volume of these particles was calculated to be 204 nm^3 and their surface area is 312 nm^2. EDX measurements were performed after 7000 cycles and the amount of Pt and Ru was quantified. On average 33 ± 3 atom% Ru and 67 ± 3 atom% Pt are detected. Even though not specifically measured on the Pt/Ru catalyst morphology displayed in Fig. 7a, similar Pt/Ru catalyst agglomerates were found to be composed of ca. 65–75 atom% Ru and 25–35 atom% Pt in the as-prepared state.

This experiment demonstrates that the Pt/Ru catalyst is stable in the simulated FC operation in the first 2000 cycles although the voltage used is larger than the ones which are typically applied in a real fuel cell stack (<0.5 V_{RHE}). A possible reason is, that the catalyst material is stabilized in the form of the agglomerate. Also Yamada et al. [50] found the stability of the Pt/Ru alloy improved with a higher amount of Ru inserted. However with ongoing FC operation simulation, a severe dissolution is observed and the amount of Ru decreases from ca. 75 atom% (Pt/Ru ratio of 0.33) to 33 atom% (Pt/Ru ratio of ca. 2) with ongoing simulated operation time (Fig. 7c). This is in accordance to literature where the long-term stability of Pt/Ru is reported to be low and a preferential dissolution of Ru occurred [69,70].

Summary

The operation related stability of the catalyst material is counted among the key factors to guarantee a reliable and long-term stable fuel cell performance. Indications of the weakest points of the catalyst NPs during starting up, long-term operation and ramping down of the fuel cell help to continue with targeted fuel cell optimization. The focus of the present work lies on the catalyst performance and degradation dependency during start-stop cycling, when high voltages are present at the anode. An in-depth analysis via TEM and STEM reveal that the Pt/Ru catalyst in the as-prepared sample exhibits different shapes: spherical nm-sized particles and bigger sized networks which are interconnected chains of nanoparticles. The particles possess a slightly distorted fcc

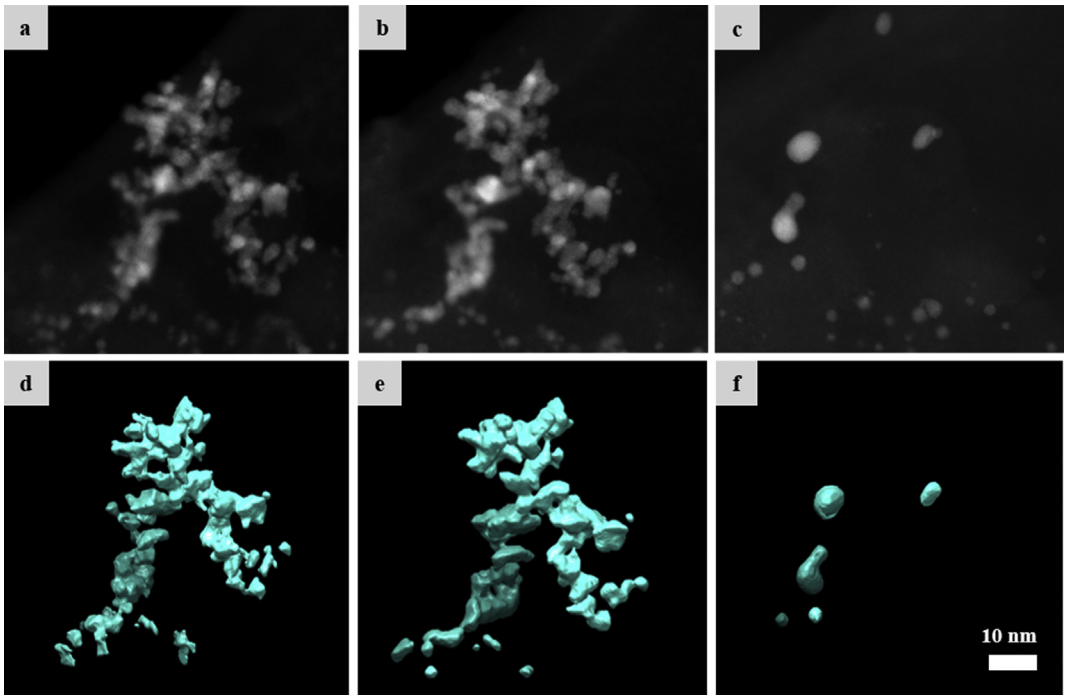

Fig. 7 – HAADF STEM micrographs of a bigger sized Pt/Ru catalyst morphology formed by polycrystalline chains of interconnected nanoparticles a) in the as prepared state; b) after 2000 cycles and c) after 7000 cycles in the potential range [0–1.2] V_{RHE}. The scalebar is the same in all images. d), e), f) are the corresponding electron tomography reconstructions.

lattice although locally changing Ru contents in the range of 14.8 atom% up to 87.9 atom% are present. The catalyst's stability is investigated by combining IL-TEM and cyclic voltammetry measurements with a focus on the effect of the maximum potential value in the CV experiment. The Pt/Ru catalyst alloys show an intensified degradation behavior when the maximum potential value is set to 1.2 V_{RHE}. In the extreme case, the major part of the catalyst dissolved. When the potential cycling range is decreased to [0–1.0] V_{RHE}, the stability of the catalyst improved significantly. This could be observed in overview areas and on single Pt/Ru catalyst morphologies. Changes of the catalyst were investigated up to 25000 potential cycles. Despite the high stability observed in the STEM micrographs, cyclic voltammograms revealed a change in the CO-stripping behavior that is attributed to the change in surface composition as the dissolution of Ru is favored over the dissolution of Pt. Indeed, the formation of a second peak at higher potentials and the vanishing peak at lower potentials indicates a loss of Ru in accordance to EDX measurements. Dissolution/dealloying is found to be the main degradation mechanism and especially in the beginning of the electrochemical treatment also agglomeration and Ostwald ripening are taking place. Particle detachment is only occasionally observed. Generally, Ru proves to be less stable during the electrochemical treatment. However, its presence in the Pt/Ru catalyst alloy accounts for an easier removal of CO from the surface of Pt as demonstrated by a lower CO stripping voltage. While this study was focusing on the stability of Pt/Ru–C under start-stop conditions, we intend to investigate also the stability during regular operation (constant current density in the standard operation range and elevated temperatures) in a follow-up work to unravel the weighting of the degradation mechanisms that differ in continuous und dynamic fuel cell operation modes.

Table 3 – Volume and accessible surface area of the catalyst network presented in Fig. 7 in the as-prepared state and after 2000 and 7000 potential cycles in the range of [0–1.2]V_{RHE}.

	as-prepared	2000 cycles	7000 cycles
Volume [nm^3]	3770	3706	204
Surface area [nm^2]	5248	4428	312

Funding sources

This work was supported by the German Federal Ministry for Economy and Energy within the program ZIM-KOOP (KF2001502ZG4).

Acknowledgement

The authors thank Benjamin Breitbach for the XRD measurements and Scott Schmeits for his guidance and technical support.

Appendix A. Supplementary data

Supplementary data related to this article can be found at http://dx.doi.org/10.1016/j.ijhydene.2017.08.108.

REFERENCES

[1] Shao M, Chang Q, Dodelet J-P, Chenitz R. Recent advances in electrocatalysts for oxygen reduction reaction. Chem Rev 2016;116:3594–657.

[2] Meier JC, Galeano C, Katsounaros I, Topalov AA, Kostka A, Schuth F, et al. Degradation mechanisms of Pt/C fuel cell catalysts under simulated start-stop conditions. Acs Catal 2012;2:832–43.

[3] Borup R, Meyers J, Pivovar B, Kim YS, Mukundan R, Garland N, et al. Scientific aspects of polymer electrolyte fuel cell durability and degradation. Chem Rev 2007;107:3904–51.

[4] Oh H-S, Lee J-H, Kim H. Electrochemical carbon corrosion in high temperature proton exchange membrane fuel cells. Int J Hydrogen Energy 2012;37:10844–9.

[5] Pizzutilo E, Geiger S, Grote J-P, Mingers A, Mayrhofer KJJ, Arenz M, et al. On the need of improved accelerated degradation protocols (ADPs): examination of platinum dissolution and carbon corrosion in half-cell tests. J Electrochem Soc 2016;163:F1510–4.

[6] Schulenburg H, Schwanitz B, Linse N, Scherer GG, Wokaun A, Krbanjevic J, et al. 3D imaging of catalyst support corrosion in polymer electrolyte fuel cells. J Phys Chem C 2011;115:14236–43.

[7] Hengge KA, Heinzl C, Perchthaler M, Geiger S, Mayrhofer KJJ, Scheu C. Growth of porous platinum catalyst structures on tungsten oxide support materials: a new design for electrodes. Cryst Growth Des 2017;17:1661–8.

[8] Heinzl C, Hengge KA, Perchthaler M, Hacker V, Scheu C. Insight into the degradation of HT-PEMFCs containing tungsten oxide catalyst support material for the anode. J Electrochem Soc 2015;162:F280–90.

[9] Perchthaler M, Ossiander T, Juhart V, Mitzel J, Heinzl C, Scheu C, et al. Tungsten materials as durable catalyst supports for fuel cell electrodes. J Power Sources 2013;243:472–80.

[10] Binninger T, Fabbri E, Kötz R, Schmidt TJ. Determination of the electrochemically active surface area of metal-oxide supported platinum catalyst. J Electrochem Soc 2014;161:H121–8.

[11] Sharma S, Pollet BG. Support materials for PEMFC and DMFC electrocatalysts—a review. J Power Sources 2012;208:96–119.

[12] Meier JC, Galeano C, Katsounaros I, Witte J, Bongard HJ, Topalov AA, et al. Design criteria for stable Pt/C fuel cell catalysts. Beilstein J Nanotechnol 2014;5:44–67.

[13] Meier JC, Katsounaros I, Galeano C, Bongard HJ, Topalov AA, Kostka A, et al. Stability investigations of electrocatalysts on the nanoscale. Energy Environ Sci 2012;5:9319–30.

[14] Mayrhofer KJJ, Ashton SJ, Meier JC, Wiberg GKH, Hanzlik M, Arenz M. Non-destructive transmission electron microscopy study of catalyst degradation under electrochemical treatment. J Power Sources 2008;185:734–9.

[15] Mayrhofer KJJ, Meier JC, Ashton SJ, Wiberg GKH, Kraus F, Hanzlik M, et al. Fuel cell catalyst degradation on the nanoscale. Electrochem Commun 2008;10:1144–7.

[16] Wu B, Zhao M, Shi W, Liu W, Liu J, Xing D, et al. The degradation study of Nafion/PTFE composite membrane in PEM fuel cell under accelerated stress tests. Int J Hydrogen Energy 2014;39:14381–90.

[17] Liu J, Zhou Z, Zhao X, Xin Q, Sun G, Yi B. Studies on performance degradation of a direct methanol fuel cell (DMFC) in life test. Phys Chem Chem Phys 2004;6:134–7.

[18] Shao-Horn Y, Sheng WC, Chen S, Ferreira PJ, Holby EF, Morgan D. Instability of supported platinum nanoparticles in low-temperature fuel cells. Top Catal 2007;46:285–305.

[19] Komanicky V, Chang KC, Menzel A, Markovic NM, You H, Wang X, et al. Stability and dissolution of platinum surfaces in perchloric acid. J Electrochem Soc 2006;153:B446–51.

[20] Cherevko S, Keeley GP, Geiger S, Zeradjanin AR, Hodnik N, Kulyk N, et al. Dissolution of platinum in the operational range of fuel cells. ChemElectroChem 2015;2:1471–8.

[21] Takei C, Kakinuma K, Kawashima K, Tashiro K, Watanabe M, Uchida M. Load cycle durability of a graphitized carbon black-supported platinum catalyst in polymer electrolyte fuel cell cathodes. J Power Sources 2016;324:729–37.

[22] Bi W, Gray GE, Fuller TF. PEM fuel cell Pt/C dissolution and deposition in nafion electrolyte. Electrochem Solid State Lett 2007;10:B101–4.

[23] Zhang S, Yuan X-Z, Hin JNC, Wang H, Friedrich KA, Schulze M. A review of platinum-based catalyst layer degradation in proton exchange membrane fuel cells. J Power Sources 2009;194:588–600.

[24] Ohma A, Suga S, Yamamoto S, Shinohara K. Phenomenon analysis of PEFC for automotive Use(1) Membrane degradation behavior during OCV hold test. ECS Trans 2006;3:519–29.

[25] Kim L, Chung CG, Sung YW, Chung JS. Dissolution and migration of platinum after long-term operation of a polymer electrolyte fuel cell under various conditions. J Power Sources 2008;183:524–32.

[26] Yasuda K, Taniguchi A, Akita T, Ioroi T, Siroma Z. Platinum dissolution and deposition in the polymer electrolyte membrane of a PEM fuel cell as studied by potential cycling. Phys Chem Chem Phys 2006;8:746–52.

[27] Xie J, Wood DL, More KL, Atanassov P, Borup RL. Microstructural changes of membrane electrode assemblies during PEFC durability testing at high humidity conditions. J Electrochem Soc 2005;152:A1011–20.

[28] Zhao M, Shi W, Wu B, Liu W, Liu J, Xing D, et al. Analysis of carbon-supported platinum through potential cycling and potential-static holding. Int J Hydrogen Energy 2014;39:13725–37.

[29] Hengge K, Heinzl C, Perchthaler M, Varley D, Lochner T, Scheu C. Unraveling micro- and nanoscale degradation processes during operation of high-temperature polymer-electrolyte-membrane fuel cells. J Power Sources 2017;364:437–48.

[30] Ferreira PJ, la O' GJ, Shao-Horn Y, Morgan D, Makharia R, Kocha S, et al. Instability of Pt/C electrocatalysts in proton exchange membrane fuel cells: a mechanistic investigation. J Electrochem Soc 2005;152:A2256–71.

[31] Schlögl K, Mayrhofer KJJ, Hanzlik M, Arenz M. Identical-location TEM investigations of Pt/C electrocatalyst degradation at elevated temperatures. J Electroanal Chem 2011;662:355–60.

[32] Pizzutilo E, Freakley SJ, Geiger S, Baldizzone C, Mingers A, Hutchings GJ, et al. Addressing stability challenges of using bimetallic electrocatalysts: the case of gold-palladium nanoalloys. Catal Sci Technol 2017;7:1848–56.

[33] Mezzavilla S, Baldizzone C, Swertz A-C, Hodnik N, Pizzutilo E, Polymeros G, et al. Structure–activity–stability relationships for space-confined Pt_xNi_y nanoparticles in the oxygen reduction reaction. ACS Catal 2016;6:8058–68.

[34] Hasché F, Oezaslan M, Strasser P. Activity, stability, and degradation mechanisms of dealloyed $PtCu_3$ and $PtCo_3$ nanoparticle fuel cell catalysts. ChemCatChem 2011;3:1805–13.

[35] Strasser P, Koh S, Anniyev T, Greeley J, More K, Yu C, et al. Lattice-strain control of the activity in dealloyed core–shell fuel cell catalysts. Nat Chem 2010;2:454–60.
[36] Mani P, Srivastava R, Strasser P. Dealloyed binary PtM_3 (M = Cu, Co, Ni) and ternary $PtNi_3M$ (M = Cu, Co, Fe, Cr) electrocatalysts for the oxygen reduction reaction: performance in polymer electrolyte membrane fuel cells. J Power Sources 2011;196:666–73.
[37] Ehteshami SMM, Chan SH. A review of electrocatalysts with enhanced CO tolerance and stability for polymer electrolyte membrane fuel cells. Electrochim Acta 2013;93:334–45.
[38] Lopes PP, Ticianelli EA. The CO tolerance pathways on the Pt–Ru electrocatalytic system. J Electroanal Chem 2010;644:110–6.
[39] Russell AE, Ball SC, Maniguet S, Thompsett D. Unravelling the complexities of CO_2 tolerance at PtRu/C and PtMo/C. J Power Sources 2007;171:72–8.
[40] Lopes PP, Freitas KS, Ticianelli EA. CO tolerance of PEMFC anodes: mechanisms and electrode designs. Electrocatalysis 2010;1:200–12.
[41] Mitchell PCH, Wolohan P, Thompsett D, Cooper SJ. Experimental and theoretical studies of fuel cell catalysts: density functional theory calculations of H_2 dissociation and CO chemisorption on fuel cell metal dimers. J Mol Catal A Chem 1997;119:223–33.
[42] Xie J, Zhang Q, Gu L, Xu S, Wang P, Liu J, et al. Ruthenium–platinum core–shell nanocatalysts with substantially enhanced activity and durability towards methanol oxidation. Nano Energy 2016;21:247–57.
[43] Gasteiger HA, Markovic N, Ross PN, Cairns EJ. Carbon monoxide electrooxidation on well-characterized platinum-ruthenium alloys. J Phys Chem 1994;98:617–25.
[44] Gasteiger HA, Marković N, Ross PN, Cairns EJ. Electro-oxidation of small organic molecules on well-characterized Pt-Ru alloys. Electrochim Acta 1994;39:1825–32.
[45] Camara GA, Giz MJ, Paganin VA, Ticianelli EA. Correlation of electrochemical and physical properties of PtRu alloy electrocatalysts for PEM fuel cells. J Electroanal Chem 2002;537:21–9.
[46] McBreen J, Mukerjee S. In situ X-Ray absorption studies of a Pt-Ru electrocatalyst. J Electrochem Soc 1995;142:3399–404.
[47] Christoffersen E, Liu P, Ruban A, Skriver HL, Nørskov JK. Anode materials for low-temperature fuel cells: a density functional theory study. J Catal 2001;199:123–31.
[48] Liu P, Nørskov JK. Kinetics of the anode processes in PEM fuel cells – the promoting effect of Ru in PtRu anodes. Fuel Cells 2001;1:192–201.
[49] Wyckoff RWG. The structure of crystals. 2nd ed. New York: Interscience Publishers; 1963.
[50] Yamada H, Shimoda D, Matsuzawa K, Tasaka A, Inaba M. Stability of Pt-Ru/C catalysts: effects of Ru content. ECS Trans 2007;11:325–34.
[51] Hutchinson JM. Solubility relationships in the ruthenium-platinum system. Platin Met Rev 1972;16:88–90.
[52] Muthuswamy N, de la Fuente JLG, Tran DT, Walmsley J, Tsypkin M, Raaen S, et al. Ru@Pt core–shell nanoparticles for methanol fuel cell catalyst: control and effects of shell composition. Int J Hydrogen Energy 2013;38:16631–41.
[53] Wang J-J, Liu Y-T, Chen IL, Yang Y-W, Yeh T-K, Lee CH, et al. Near-monolayer platinum shell on core–shell nanocatalysts for high-performance direct methanol fuel cell. J Phys Chem C 2014;118:2253–62.
[54] Alayoglu S, Zavalij P, Eichhorn B, Wang Q, Frenkel AI, Chupas P. Structural and architectural evaluation of bimetallic nanoparticles: a case study of Pt–Ru Core–Shell and alloy nanoparticles. ACS Nano 2009;3:3127–37.
[55] Sánchez-Padilla NM, Montemayor SM, Torres LA, Rodríguez Varela FJ. Fast synthesis and electrocatalytic activity of M@Pt (M = Ru, Fe3O4, Pd) core–shell nanostructures for the oxidation of ethanol and methanol. Int J Hydrogen Energy 2013;38:12681–8.
[56] Ohma A, Shinohara K, Iiyama A, Yoshida T, Daimaru A. Membrane and catalyst performance targets for automotive fuel cells by FCCJ membrane, catalyst, MEA WG. ECS Trans 2011;41:775–84.
[57] Taniguchi A, Akita T, Yasuda K, Miyazaki Y. Analysis of electrocatalyst degradation in PEMFC caused by cell reversal during fuel starvation. J Power Sources 2004;130:42–9.
[58] Liang D, Shen Q, Hou M, Shao Z, Yi B. Study of the cell reversal process of large area proton exchange membrane fuel cells under fuel starvation. J Power Sources 2009;194:847–53.
[59] Taniguchi A, Akita T, Yasuda K, Miyazaki Y. Analysis of degradation in PEMFC caused by cell reversal during air starvation. Int J Hydrogen Energy 2008;33:2323–9.
[60] Gilbert P. Iterative methods for the three-dimensional reconstruction of an object from projections. J Theor Biol 1972;36:105–17.
[61] Lakshminarayanan AV, Lent A. Methods of least squares and SIRT in reconstruction. J Theor Biol 1979;76:267–95.
[62] Gregor J, Benson T. Computational analysis and improvement of SIRT. IEEE Trans Med Imaging 2008;27:918–24.
[63] Batenburg KJ, Bals S, Sijbers J, Kübel C, Midgley PA, Hernandez JC, et al. 3D imaging of nanomaterials by discrete tomography. Ultramicroscopy 2009;109:730–40.
[64] Zürner A, Döblinger M, Cauda V, Wei R, Bein T. Discrete tomography of demanding samples based on a modified SIRT algorithm. Ultramicroscopy 2012;115:41–9.
[65] Mayrhofer KJJ, Strmcnik D, Blizanac BB, Stamenkovic V, Arenz M, Markovic NM. Measurement of oxygen reduction activities via the rotating disc electrode method: from Pt model surfaces to carbon-supported high surface area catalysts. Electrochim Acta 2008;53:3181–8.
[66] Antolini E. The problem of Ru dissolution from Pt–Ru catalysts during fuel cell operation: analysis and solutions. J Solid State Electrochem 2011;15:455–72.
[67] Baldizzone C, Gan L, Hodnik N, Keeley GP, Kostka A, Heggen M, et al. Stability of dealloyed porous Pt/Ni nanoparticles. ACS Catal 2015;5:5000–7.
[68] Dinh HN, Ren X, Garzon FH, Piotr Z, Gottesfeld S. Electrocatalysis in direct methanol fuel cells: in-situ probing of PtRu anode catalyst surfaces. J Electroanal Chem 2000;491:222–33.
[69] Park Y, Lee B, Kim C, Oh Y, Nam S, Park B. The effects of ruthenium-oxidation states on Ru dissolution in PtRu thin-film electrodes. J Mater Res 2009;24:2762–6.
[70] Henry PA, Guétaz L, Pélissier N, Jacques P-A, Escribano S. Structural and chemical analysis by transmission electron microscopy of Pt–Ru membrane precipitates in proton exchange membrane fuel cell aged under reformate. J Power Sources 2015;275:312–21.